Journal of Photochemistry & Photobiology, A: Chemistry 433 (2022) 114171

Contents lists available at ScienceDirect

Journal of Photochemistry & Photobiology, A: Chemistry

journal homepage: www.elsevier.com/locate/jphotochem

Photodehydration mechanisms of quinone methide formation from 2-naphthol derivatives

Mateo Forjan [a], Silvije Vdović [a,*], Marina Šekutor [b], Đani Škalamera [b,1], Piotr Kabaciński [c], Giulio Cerullo [c]

[a] Institute of Physics, Bijenička cesta 46, 10 000 Zagreb, Croatia
[b] Department of Organic Chemistry and Biochemistry, Ruđer Bošković Institute, Bijenička cesta 54, 10 000 Zagreb, Croatia
[c] IFN-CNR, Dipartimento di Fisica, Politecnico di Milano, Piazza Leonardo da Vinci 32, I-20133 Milano, Italy

A B S T R A C T

Photogeneration of quinone methides (QM) from 3-hydroxymethyl-2-naphthol (**1**) and 3-(2-hydroxy-2-adamantyl)-2-naphthol (**2**) was investigated using femtosecond and nanosecond transient absorption spectroscopy and supported with theoretical analysis of possible reaction pathways. Our results indicate that adamantylnaphthol **2** after UV excitation undergoes a non-adiabatic excited state intramolecular proton transfer coupled with dehydration *via* a conical intersection, delivering the corresponding QM (S_0) within 1 ns. Surprisingly, in naphthol **1** on femtosecond time scale only formation of radical cation and solvated electrons was observed where the photoionization is a competing process not connected to the photochemical reaction of QM formation. Radical cations decay fast (45 ps) due to the back electron transfer. By quenching with ascorbate we identified phenoxyl radicals as a QM precursor, which are formed in a slower H-transfer reaction taking place on nanosecond time scale. Our combined experimental and theoretical investigation points to a polycyclic substituent effect, which profoundly changes the photochemical reaction pathway.

1. Introduction

Quinone methides (QMs) are important intermediates in the chemistry and photochemistry of phenols [1]. They attracted considerable attention over the past two decades due to their biological activity [2,3] and increasing number of applications in organic synthesis [4,5]. The biological activity of QMs is mostly connected to their reactivity with polynucleotides [6,7], and they have found application as agents capable of reversibly cross-linking DNA [8–10] and alkylating G-quadruplexes [11–14]. Moreover, their ability to alkylate amino acids [15] and proteins [16–19] has also been demonstrated. Due to the high reactivity of QMs, they cannot be stored and have to be generated *in situ* prior to their use [20]. In that context, photochemical methods provide significant advantages when compared to standard thermal reactions, since they allow for QM generation under mild conditions, compatible with biological systems, and spatial and temporal control of the process [21,22]. One of the commonly used methods for the photogeneration of QMs is photodehydration of suitably substituted phenols [23,24].

The photodehydration reaction and formation of QMs has been demonstrated for derivatives of 2-naphthol [25]. Popik *et al.* have shown that the QMs generated from naphthols have applicability in the fluorescent staining of proteins [17], as well as in lithography and surface modifications [26–29]. It was reported that photodehydration of 2-naphthol derivative **1** takes place *via* a benzoxete derivative **1-BO**, which on the microsecond time scale undergoes ring opening to QM derivative **1-QM** (Scheme 1) [25]. On the other hand, dehydration on a similar adamantane derivative **2** takes place much faster (Scheme 2), and the corresponding **2-QM** is formed within few nanoseconds [30]. Moreover, it was demonstrated that incorporation of an adamantane scaffold into chromophores can lead to a change of photophysical properties and photochemical reactivity. Whereas 2-hydroxymethylphenol undergoes ultrafast adiabatic dehydration to QM on the S_1 excited state potential energy surface [24], the dehydration in the corresponding adamantyl derivative proceeds *via* a conical intersection (CI), delivering the QM directly in S_0 [31].

For the applications of QMs, it is important to characterize all intermediates in their formation and obtain information of their formation dynamics, since intermediates can interact with different molecules and lead to undesired effects such as cytotoxicity in biological systems or malfunctions in implementations related to material science. Consequently, we undertook investigations of photodehydration in **1** and **2** on the ultrafast time scale by femtosecond transient absorption (fs-TA), and nanosecond laser flash photolysis (LFP) to unravel hitherto undisclosed mechanistic details of these important photochemical reactions. The

* Corresponding author.
[1] Present address: Department of Chemistry, Faculty of Science, University of Zagreb, Horvatovac 102A, 10 000 Zagreb, Croatia.

https://doi.org/10.1016/j.jphotochem.2022.114171
Received 30 January 2022; Received in revised form 4 July 2022; Accepted 22 July 2022
Available online 26 July 2022
1010-6030/© 2022 Elsevier B.V. All rights reserved.

experimental observations are corroborated by computations using time-dependent density functional theory (TD-DFT) methods. We provide an alternative mechanistic scenario for the formation of **1-QM** that involves phenoxyl radicals as intermediates. Conversely, we find that photodehydration of **2** takes place without additional intermediates and **2-QM** is formed directly from the singlet excited state of **2** *via* a CI.

2. Experimental and computational methods

2.1. Materials

Synthesis of both naphthol derivatives has been described previously [25,30]. Naphthol **1** was dissolved in CH_3CN-H_2O (1:1) in the concentration $c = 1.07 \times 10^{-3}$ M, which corresponded to the absorbance $A = 3$ at the 267 nm excitation wavelength measured in a cuvette with 1 cm path, while for the second set of measurements using lower fluence from sub-20-fs pump pulses, in order to have a reasonable level of the fs-TA signal, the concentration was increased to $c = 5.00 \times 10^{-3}$ M. Adamantylnaphthol **2**, being less soluble in aqueous media than **1**, was dissolved in CH_3CN-H_2O (3:1) in the concentration $c = 3.02 \times 10^{-4}$ M, which corresponds to the absorbance $A = 0.9$ at 267 nm in a cuvette with 1 cm path. In fs-TA and LFP measurements acetonitrile of HPLC purity and mQ H_2O (Millipore) were used. All measurements were performed at ambient temperature (22–25 °C).

2.2. Femtosecond transient absorption (fs-TA)

Photochemistry of QM generation from naphthols on ultrafast time scales was investigated on a homebuilt fs-TA experimental setup which was described previously [31]. The setup was based on a Ti:sapphire regenerative amplifier system (Spitfire, Spectra-Physics) operating at 800 nm and delivering 120 fs pulses at 1 kHz repetition frequency. The pump beam is generated *via* third harmonic generation where the fundamental 800 nm pulses are first frequency doubled to 400 nm and then mixed with the leftover 800 nm to give 267 nm pulses. The energy of the pump pulses was set to 260 nJ per pulse for **2** and 200 nJ per pulse for **1**. Pump beam diameter at the focal plane was 150 μm, resulting in fluence of 1.47 mJ cm^{-2} for **2** and 1.13 mJ cm^{-2} for **1**. Samples were flown in a 0.5 mm path length quartz flow cell connected to a micro-annular gear pump. The probe beam was sent to a retroreflector set on a 20 cm long delay stage. A white light continuum (WLC) was obtained by focusing the beam to a 3 mm thick CaF_2 window. The generated WLC was collimated and the remaining fundamental light was filtered out by a UV grade fused silica high reflectivity back side polished mirror for 800 nm (Eksma Optics 042–0800-i0) after which the probe beam was focused in a flow cell to a diameter of approximately 60 μm. The spectrum of the filtered WLC ranged from 325 nm to 660 nm. After the flow cell, the probe beam was collimated by a spherical mirror and sent to a homemade spectrometer with the line rate > 1 kHz and 16-bit analog to digital conversion. Due to a high line rate, spectral intensities were read out in the single-shot regime. Instrument response function (IRF) of ≈250 fs was determined from the measurements in a pure solvent, which showed only coherent artifacts such as two-photon absorption and cross-phase modulation (XPM) to which we fit a Gaussian and its time derivatives [32].

The second, high temporal resolution broadband fs-TA spectrometer used to reveal early ultrafast dynamics in **2** has been described in detail elsewhere [33]. Briefly, the setup is based on an amplified Ti:sapphire laser (Coherent Libra). The pump pulses are generated by second harmonic generation of a visible non-collinear optical parametric amplifier (NOPA) in a 20-μm-thick β-barium borate crystal, resulting in sub-20-fs pulses in the UV tunable between 260 nm and 290 nm. For WLC a small fraction of the fundamental laser output is focused onto a 3-mm-thick CaF_2 plate. The pump and the probe beams are separately and non-collinearly focused on the sample at approximately 5° by two UV enhanced aluminum spherical mirrors. The fluence of the pump beam with energy of 113 nJ was 1 mJ cm^{-2}. To increase the signal level parallel polarizations of pump and probe beams were used for fs-TA measurements with sub-50-fs resolution. The transmitted probe, selected by an iris, is focused on the entrance slit of a spectrometer (SP2300 Princeton Instruments, Acton, MA, USA) equipped with a CCD detector, with spectral resolution of 0.5 nm, and a read-out electronics (Entwicklungsbuero EB Stresing, Berlin, Germany) capable of single-shot measurement of the probe spectrum at the full 1-kHz laser repetition rate. Measurements were taken by overlapping the pump and probe pulses on a 1 mm optical path-length spectrophotometric quartz flow cell. In both experiments the flow cell system was pumped at a rate that ensured a fresh sample volume for each pump pulse.

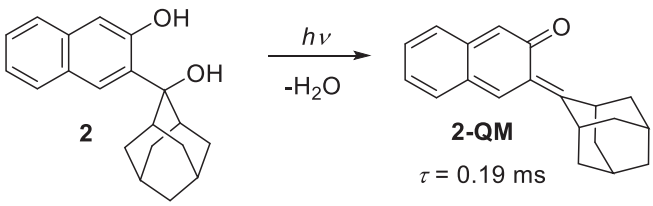

Scheme 2. Photodehydration of **2** and formation of the corresponding **2-QM** [30].

2.3. Laser flash photolysis (LFP)

The measurements were performed on a LP980 Edinburgh Instruments spectrometer. For the excitation a Qsmart Q450 Quantel Nd:YAG laser was used with the fourth harmonic at 266 nm. The energy of the laser pulse was set to 7 or 15 mJ (see the Supporting Information). Naphthols **1** and **2** were dissolved in CH_3CN-H_2O (1:1, in the presence of sodium phosphate buffer, 50 mM, pH 7.0) in the concentration $c = 9.40 \times 10^{-5}$ M, and 7.09×10^{-5} M, respectively, corresponding to an absorbance at 266 nm $A_{266} = 0.30$. Prior to the measurements, solutions were purged with a stream of argon or oxygen for 20 min. The measurements were performed at 25 °C in static cells which were frequently exchanged to remove potential artifacts from the photoproducts.

2.4. Computational methods

Geometry optimizations were performed with the GAUSSIAN16 [34] program package using the PCM(water)/ωB97XD/6–311++G(d,p) level of theory [35,36] and the obtained minima were verified by frequency computations. The PCM(water)/TD-ωB97XD/6–311++G(d,p) level of theory was used for excited state optimizations and computations of vertical excitation energies for 20 energetically lowest excited singlet states. The viability of the used TD-DFT method was supported by the

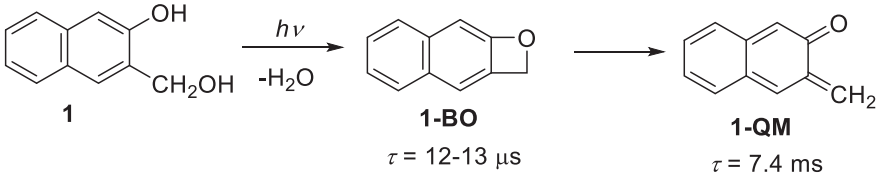

Scheme 1. Photochemical formation of **1-QM** [25].

benchmarking performed previously [24,31,37]. Conical intersection optimization scan for **1-QM**(S_0) and **2-QM**(S_0) formation was performed on the same level of theory using ORCA 4.2.0 [38,39].

3. Results and discussion

3.1. Absorption and fluorescence measurements

Naphthol derivatives **1** and **2** show two broad and structured low energy absorption bands at ≈ 275 and 325 nm, corresponding to the excitation to S_2 and S_1 state, respectively (Fig. 1 left). Upon excitation at 267 nm used in fs-TA experiments, population of the S_2 state takes place. The emission spectra are the mirror image of the lowest energy absorption band with the maxima at ≈ 355 nm (Fig. 1 right). Contrary to the typical dual emission spectra of 2-naphthol in aqueous solvent due to excited state proton transfer (ESPT) and formation of naphtholate in S_1 (425–430 nm) [40], addition of protic solvent to the solution of **1** and **2** does not change the spectra significantly. Only a shoulder can be detected at λ≈ 420 nm, which is attributed to the emission from naphtholate. Consequently, ESPT to solvent for **1** and **2** is only a minor photochemical process. Note, however, that the adiabatic formation of naphtholate in ESPT should be differentiated from the excited state intramolecular proton transfer (ESIPT) that is coupled with dehydration and delivers QM (*vide infra*). The decay times of the singlet excited state reported in the literature are 7 ns for **1** [25] and 3.0 and 6.1 ns for **2** [30].

3.2. Transient absorption measurements

Except for the measurements using sub-20 fs pump pulses that covered only initial reaction dynamics up to few ps, fs-TA measurements for both naphthol derivatives were carried out under the magic angle conditions to eliminate the possibility of rotational diffusion introducing additional anisotropy decay in the measurements, thus ensuring that the dynamics obtained in the measurements were originating from pure population effects.

3.3. Naphthol *1*

A 2D TA map, time dynamics at selected wavelengths and TA spectra at selected time delays for **1** dissolved in CH_3CN-H_2O (1:1) are shown in Fig. 2. At all probe wavelengths, we observe a positive signal (ΔOD > 0), corresponding to a photoinduced absorption (PA). Characteristic time constants were extracted using single wavelength fitting of exponential decay convolved with the IRF, described as Gaussian function, followed by the global analysis. The coherent artifacts (cross-phase modulation, two photon absorption) appearing around time zero and interfering with the population dynamics were modeled as a sum of a Gaussian and its time derivatives [32]. Fluorescence of **1** spreads from 330 nm to approximately 500 nm with fluorescence quantum yield of $\Phi_F = 0.23$ [25]. The absence of stimulated emission (SE) and ground state bleach (GSB) signals at shorter wavelengths in our measurements can be explained with the overlap of the weaker negative SE and GSB bands with a stronger positive PA band. Analysis of single wavelength fitting results, together with the results of the computational study, was used for the interpretation of global and target analysis. Results of single wavelength fitting can be found in the Supporting Information.

Global and target analysis was done using the Glotaran software [41] where several models were tested. Two models consisting of four compartments (Fig. 3) gave best fitting results that are shown in Figs. 4 and 5. It should be noted that global analysis with sequential model having four decay constants that would correspond to $S_2 \rightarrow S_1 \rightarrow RC \rightarrow R \rightarrow QM$ (RC – radical cation, R – phenoxyl radical) reaction pathway gave equally good results that we disregarded due to its unrealistic prediction (when compared to the fluorescence lifetime results) of 45 ps lifetime of the S_1 state (see Fig. S2).

Model 1 (Fig. 4) starts with **1**(S_2), which in parallel on the ultrafast scale yields radical cation (720 fs) and undergoes IC to **1**(S_1) (430 fs). The signal at 322 nm exhibiting a slightly delayed rise and slow nanosecond decay is ascribed to excited state absorption (ESA) from **1**(S_1). Furthermore, the signal at 570 nm was assigned to the radical cation of **1**, formed by photoionization. The assignment is based on the previously published spectrum of 2-naphthol radical cation with a lifetime of 1.5 μs, formed by pulse radiolysis in the presence of butyl chloride [42]. The TA band at 380 nm that starts to be visible after few picoseconds and experiences a slight blueshift is assigned to the radical cation as well, based on previous arguments in the interpretation of the 570 nm spectral band. The radical cation undergoes vibrational relaxation with the associated time constant of 3.7 ps, after which it decays with the time constant of 45 ps. Deprotonation of the radical cation normally proceeds on longer time scales on the order of 0.1–1 ns [43]. However, such time constant was not revealed in our global analysis of **1**, and the observed decay of the radical cation was faster. Furthermore, evolution of a new transient band that could be assigned to phenoxyl radical (formed by deprotonation) was not observed in the fs-TA data. On the picosecond time scale the observed transients decayed without formation of any new species. Note, however, that the phenoxyl radical was detected with a longer delay and observed in the LFP experiments (*vide infra*). Based on detailed analysis of possible reaction pathways, the dynamics taking place in 45 ps can be explained as reduction of the radical cation with solvated electrons in a back electron transfer and formation of the initial naphthol molecule in its ground state (see Scheme 4). Population in **1**(S_1) decays much slower, with a time constant of 2.5 ns. We note that this lifetime is lower by factor of 3 than the value obtained by fluorescence lifetime measurement. This discrepancy can be explained by the fact that TA measurements only cover time window up to 1.1 ns and, as a result, there is a large uncertainty in the determination of all decay time constants longer than 1 ns. The species associated spectrum (SAS) corresponding to **1**(S_2) is shown as a SAS_1 in Fig. 4 and it consists of a band peaked at 360 nm which arises with the time resolution of our experimental setup. Vibrational relaxation of radical cation is manifested as a

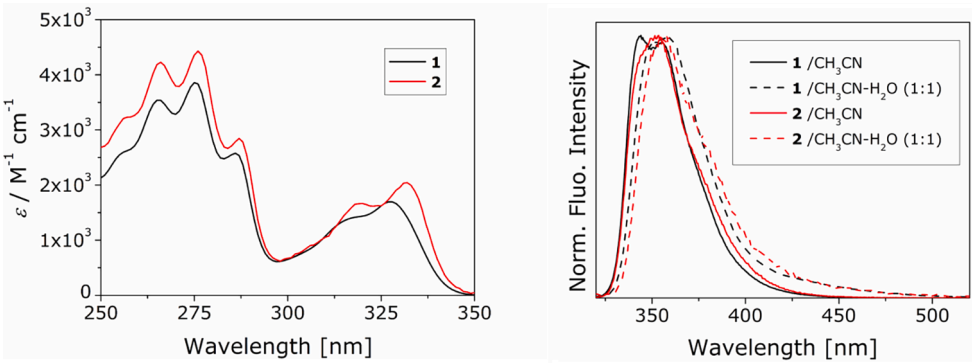

Fig. 1. Absorption spectra of **1** and **2** in CH_3CN (left), and normalized emission spectra (λ_{exc} = 310 nm) in CH_3CN and CH_3CN-H_2O (1:1) (right).

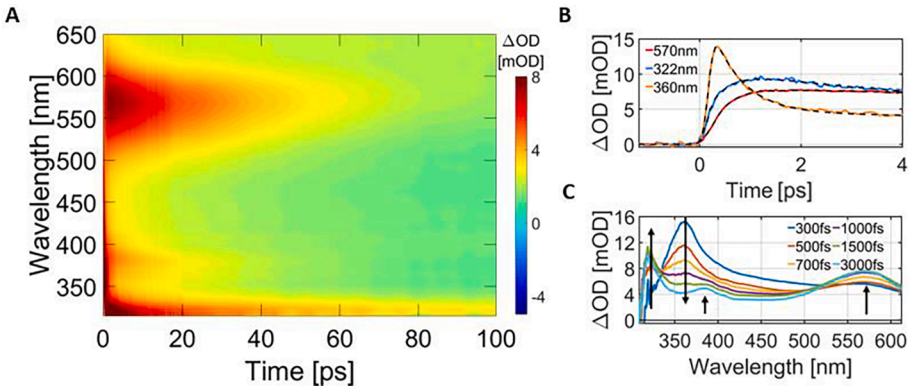

Fig. 2. (A) 2D TA map of **1**, (B) corresponding time dynamics together with the fitting results shown for three selected wavelengths with subtracted coherent artifact modeled as Gaussian and its derivatives and (C) TA spectra shown for selected time delays where arrows point to the direction of the spectral evolution in time.

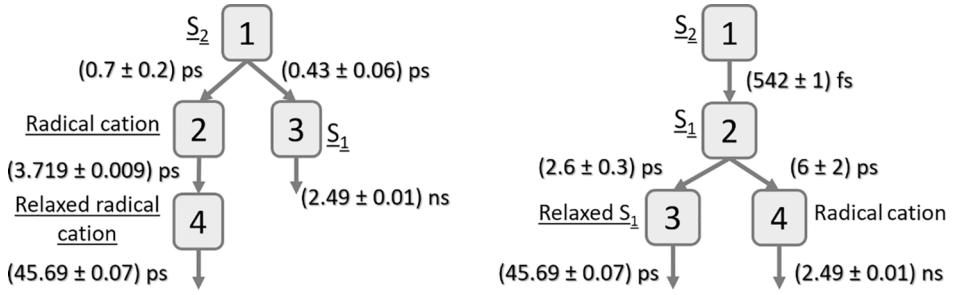

Fig. 3. Two models used in target analysis that produced best fitting results of fs-TA data for **1**.

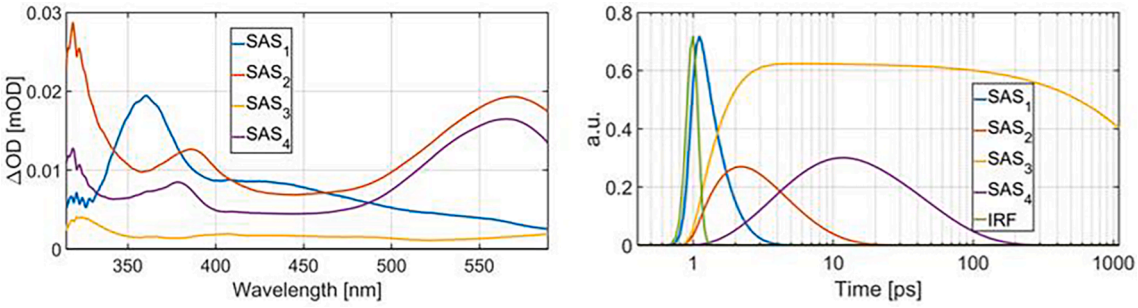

Fig. 4. Results of target analysis for **1** obtained using model 1 with four kinetic time constants. (Left) Species associated spectra (SAS) and (right) time profiles of associated SAS plotted on a logarithmic time scale.

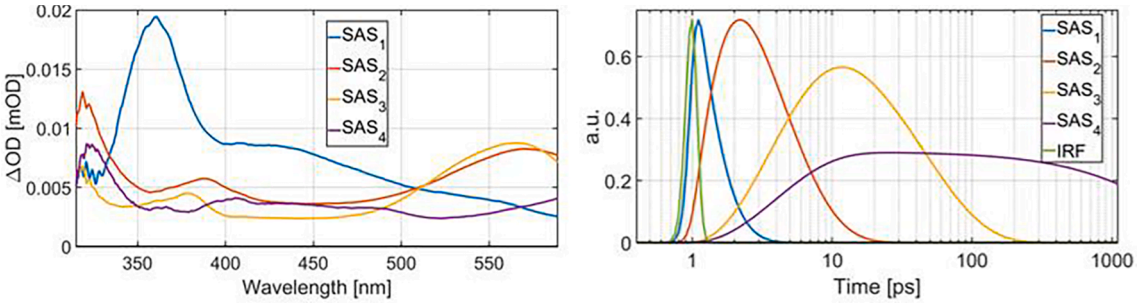

Fig. 5. Results of target analysis for **1** obtained using model 2 with four kinetic time constants. (Left) Species associated spectra (SAS) and (right) time profiles of associated SAS plotted on a logarithmic time scale.

blue shift of SAS_4 with respect to SAS_2, which represents the vibrationally hot radical cation. **1**(S_1) is shown as SAS_3, having a band centered at 320 nm with a slight indication of the presence of solvated electrons at wavelengths longer than 500 nm. This band is also present in the SAS corresponding to radical cations, indicating both species have significant absorption cross section in this spectral range. Due to slow

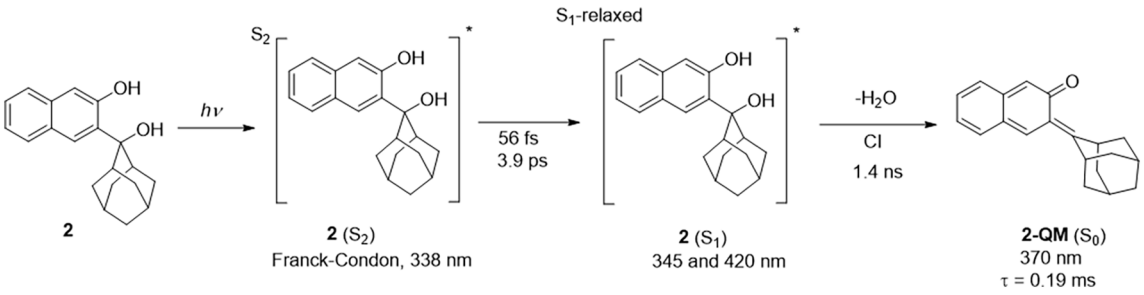

Scheme 3. Proposed mechanism of photochemical dehydration reaction of **2** resulting in direct formation of **2-QM**(S_0) *via* a CI. Note that for simplicity internal conversion process corresponding to 56 fs time constant is not graphically shown as a distinct step.

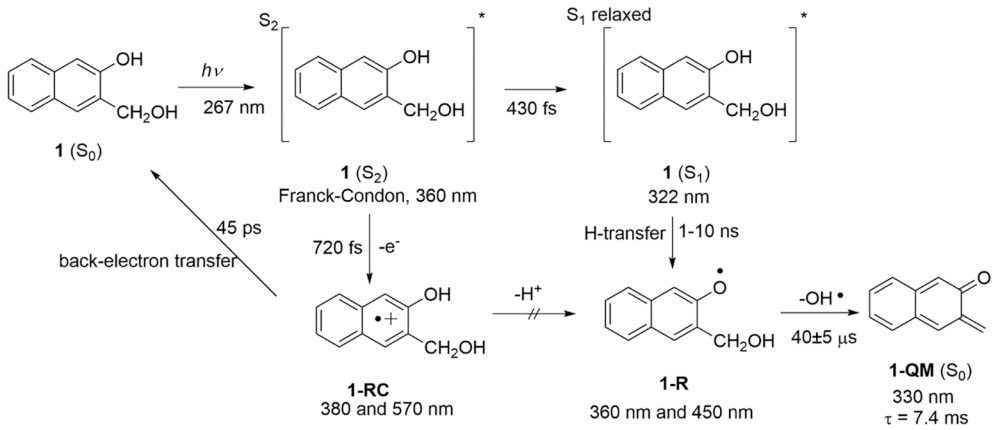

Scheme 4. Proposed mechanism of photodehydration reaction of **1** where phenoxyl radical **1-R** was identified as a QM precursor.

dynamics of solvated electrons and **1**(S_1), it was not possible to disentangle those two contributions into separate spectra. It is worth mentioning that neither of the observed PA bands should represent the triplet excited state of **1**, since the triplet–triplet absorption of 2-naphthol is located around 430 nm, [44] where our measurements show no pronounced spectral features. Furthermore, Figure S1 shows the difference between the spectra recorded under identical experimental conditions for **1** and the pure solvent. The positive signal observed above 550 nm in the spectrum of **1** points to greater concentration of solvated electrons than in the pure solvent, which in turn indicates generation of radical cations, as assumed.

Model 2 (Fig. 5) describes ultrafast IC from **1**(S_2) to vibrationally hot **1**(S_1) (543 fs) which then simultaneously vibrationally relaxes and yields the radical cation with time constants of 2.63 ps and 6.35 ps, respectively. Relaxed S_1 state then decays with the time constant of 45.7 ps while the radical cation decays much slower within 2.49 ns. Similar to model 1, the vibrational relaxation is presented as blue shift of SAS_3 with respect to SAS_2. Contrary to model 1, SAS_4 corresponding to the radical cation consists of an absorption band at 320 nm and another positive band at wavelengths longer than 500 nm. However, the 45.7 ps lifetime of **1**(S_1) obtained in model 2 is not in agreement with the value obtained by fluorescence lifetime measurements (7 ns) [25]. Thus, based on the target analysis we can discard model 2 and conclude that model 1 is a much more realistic description of the photochemistry of **1**.

3.4. *Adamantylnaphthol* ***2***

The fs-TA measurements of **2** in CH_3CN-H_2O (3:1) are strikingly

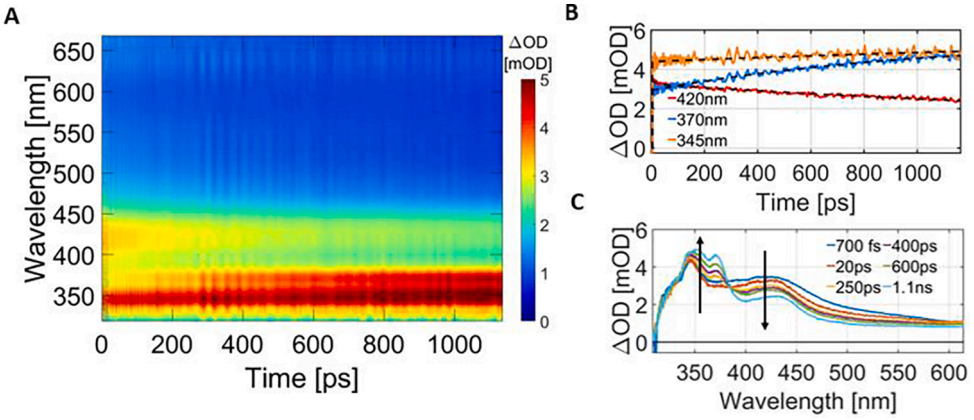

Fig. 6. (A) 2D TA map of **2**, (B) corresponding time dynamics together with the fitting results shown for three selected wavelengths and (C) TA spectra shown for selected time delays where arrows point to the direction of the spectral evolution in time.

different from those of **1**, which is at a first glance somewhat surprising since the only difference in molecular structure is the adamantane moiety which is not expected to significantly affect its photoreactivity. Results of measurements are shown in Fig. 6. Initially, right after the excitation, the TA spectrum consists of two clearly visible absorption bands peaking at 345 nm and 420 nm, which eventually narrow down to their shape shown in Fig. 6C as a red spectrum (at 20 ps time delay). After few hundreds of picoseconds, PA bands at 350 nm and 370 nm start emerging with a well-defined isosbestic point at 385 nm. The newly formed bands continue rising up to 1.1 ns, which was the last reachable point of our fs-TA experimental setup. Besides newly formed PA bands, at longer delay times an additional band emerges at 432 nm, which seems to differ from the much broader band with the maximum at 420 nm appearing right after the excitation. Fluorescence of **2** spreads from 330 nm to approximately 500 nm (Fig. 1) and the fluorescence quantum yield is $\Phi_F = 0.18$ in CH_3CN-H_20 (1:4 v/v) [30]. As in the case of **1**, the absence of SE and GSB in our measurements can be explained by overlap of a weaker SE and GSB bands with stronger positive PA bands. Similar absence of the SE was observed in case of adamantylphenol [31], which has a slightly lower fluorescence quantum yield $\Phi_F = 0.13$ [45]. It is also possible that hidden SE dynamics is at least in part responsible for the observed discrepancies in the evolution of different bands (*vide infra*).

Fig. 7A shows normalized time traces of PA bands appearing in the spectra right after the excitation (420 nm and 345 nm) after the subtraction of coherent artifacts obtained by fitting. Coherent artifacts were, as before, modeled by a Gaussian and its derivatives. Without adding any rise components, a high quality fit was obtained. IRF FWHM was a free parameter for fitting and obtained value was 248 fs at 420 nm and 246 fs at 345 nm, which coincided with the time resolution obtained from solvent measurements and confirmed that signals rise within our temporal resolution. As in the case of **1**, the excitation at 267 nm provides enough energy to populate the S_2 electronic state. Since both bands are in principle formed within the excitation fs laser pulse, we initially assign them to ESA from S_1 state of **2**. Lack of initial ultrafast decay that could be associated with the internal conversion (IC) indicates that it takes place on an ultrafast timescale, shorter than 250 fs which is the time resolution of the setup used. However, in the fs-TA experiment with sub-50-fs temporal resolution (Fig. 7B and S3) ultrafast decay at 338 nm and delayed rise at 420 nm can be seen, which we attribute to the S_2-S_1 IC, with ESA of **2**(S_2) contributing more at shorter wavelengths (338 nm). Fitting results at the 338 nm showed that signal rises within the IRF (<50 fs) followed by a 56 fs ultrafast decay, while for 420 nm the 96 fs rise time obtained by the fit is definitely slower than the temporal resolution of the experiment. Since both fs-TA setups use homemade spectrometers, there is a minor discrepancy in wavelength calibration, especially at shorter wavelengths, that causes PA bands emerging at different wavelengths (345 *vs* 338 nm).

After the population of **2**(S_1), on a longer time scale, there is an obvious relation between the rise of the PA band at 370 nm and the corresponding decay of the PA band at 420 nm taking place on the timescale of a few hundreds of picoseconds, which is also evident due to the presence of an isosbestic point (Fig. 6). We assign the peak at 370 nm to absorption band of **2-QM** (S_0), based on comparison with the spectra reported in the literature [30] and results from LFP (*vide infra*). However, the fitting results for the PA rise at 370 nm and decay at 420 nm (Fig. S4) show discrepancy, whereas they should be approximately equal if there was a pure transition from **2**(S_1) to **2-QM** (S_0). Decay time constant of 3.9 ns was obtained by the fit at 420 nm, while rise at 370 nm is much faster with a 1.4 ns time constant. It must be noted that the fitting parameters with values comparable to our 1.1 ns time window are not precisely determined. On that account the discrepancy of decay/rise time constants are most probably overemphasized by the fit. Presumably, the observed difference in the characteristic time constants for the decay at 420 nm, due to the photodehydration of **2**, and the rise at 370 nm stems from the overlapped additional PA band in that spectral region (*vide infra*, LFP data). In parallel with the appearance of the PA band at 370 nm, another signal emerges at 350 nm at later delay times. The apparent slow rise of absorption at 345 nm, where we expected to see the decay ESA from **2**(S_1), can be explained with the strong overlap with nearby QM absorption band at 350 nm.

It can be argued that the PA band centered around 432 nm that we detected on the nanosecond time scale stems from a species other than QM. For example, the 432 nm band could be an emerging triplet ESA initially overlapped with the ESA from **2**(S_1). The triplet excited state of **2** has been detected in N_2 purged CH_3CN and CH_3CN-H_2O solutions at 430–450 nm. It has a lifetime of microseconds and can be quenched by O_2 [30]. This assumption is in line with other studies that describe the triplet excited state of 2-naphthol absorbing at around 430 nm [44,46,47].

In global analysis several sequential and parallel models were tested. A sequential model with three kinetic parameters displayed the best fit in the case of **2** (Fig. 8). The corresponding evolution associated spectra (EAS) and the associated time profiles are shown in Fig. 9. First EAS consists of two bands at 345 nm and 420 nm, already assigned to ESA from **2**(S_1). It evolves to the second EAS with time constant of 3.9 ps. It can be clearly seen that the second EAS is merely slightly blue shifted and narrowed compared to the first EAS. Blue shifting of the spectrum can be explained due to the process of solvation where **2**(S_1) energy decreases as a consequence of molecular rotations in a polar solvent due to the finite dipole moment of the naphthol. Moreover, it can also occur from vibrational cooling of a hot S_1 state of **2** after IC from S_2. Spectral narrowing originates only from vibrational cooling of a hot S_1 state of **2**. Both of these phenomena occur on similar time scales and consequently cannot be distinguished from each other, so that in global analysis they

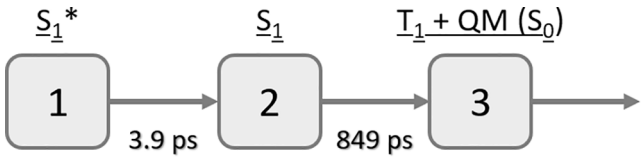

Fig. 8. Sequential model used in global analysis that produced best fitting results of fs-TA data for **2**.

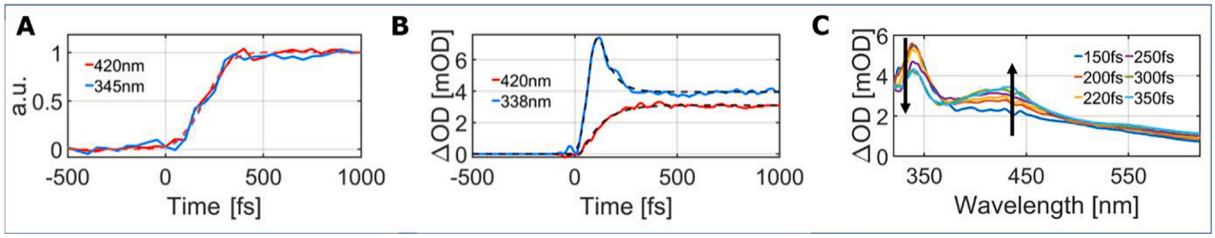

Fig. 7. Kinetic profiles together with fitting results at prominent peaks appearing in spectra of **2** right after the excitation. (A) Normalized time traces were obtained in fs-TA experiment with 250 fs temporal resolution after the subtraction of coherent artifacts modeled as a Gaussian and its time derivatives. (B) Dynamics at relevant wavelengths and (C) initial TA spectra measured in experiment with sub-50-fs temporal resolution.

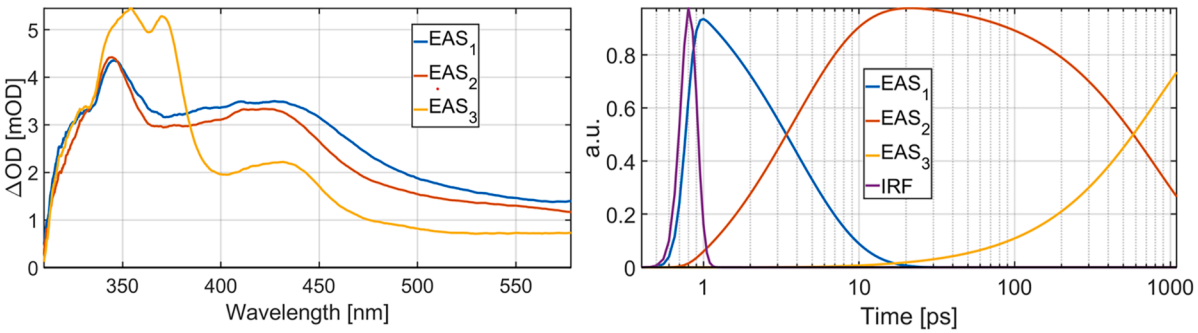

Fig. 9. Results of global analysis for **2** obtained under the assumption of a sequential model with 3 kinetic time constants. (Left) Evolution associated spectra (EAS) and (right) time profiles of associated EAS plotted on a logarithmic time scale.

give rise to one time constant and one EAS instead of two. After the vibrational cooling and solvation, the spectrum transforms with a time constant of 849 ps to the third EAS, assigned mainly to **2-QM**(S_0) absorption band. The band at 435 nm in this EAS, rising with the same constant as bands at 350 nm and 370 nm and being responsible for the slower decay of the PA signal at 420 nm, is assigned to the triplet–triplet absorption of **2**. Since in fs-TA measurements this transient is only seen at later times at the limits of the setup used, global analysis cannot recognize the difference between its dynamics and the dynamics at 370 nm, resulting in only one EAS (EAS_3) instead of two. The third time constant obtained was indefinite, and it relates to the decay of **2-QM**(S_0), whose reported lifetime was $\tau = 0.19$ ms [30].

In summary, our initial assignment of the transients is the following: both of the PA bands visible in initial spectra represent ESA from **2**(S_1), reached following an ultrafast (≈50 fs) IC from S_2. We justify this assignment by their slow decay on the nanosecond time scale. Furthermore, based on the results of computations (*vide infra*), bands rising and appearing after few hundreds of picoseconds, at 350 nm and 370 nm, correspond to absorption from **2-QM** (S_0), populated directly from **2**(S_1) *via* a CI. This signal is overlapped with the triplet–triplet absorption of **2** (T_1) at 432 nm, formed from **2**(S_1) *via* intersystem crossing.

3.5. Laser flash photolysis

LFP measurements for **1** in pure CH_3CN and CH_3CN-H_2O (1:1), shown in Fig. 10, present a smooth continuation to fs-TA measurements. Detailed analysis clearly shows how the 360 nm transient decays with a time constant of 40 ± 5 μs (for both the aqueous and non-aqueous solution) and gives rise to a PA band at 330 nm which is known to correspond to **1-QM** (S_0) [25]. Associated kinetic profiles are shown in Figure S5. Based on fs-TA experiments where we detected the naphthol radical cation, we propose an alternative assignment for the QM precursor absorbing at 360 nm to a phenoxyl radical. Namely, the phenol radical cations are known to deprotonate to phenoxyl radicals, [48] and in aqueous solvent the rate constant for the deprotonation is ≈ 0.5–5 × 10^8 s^{-1} [43], which corresponds to the time-scale of the ns-laser pulse and cannot be time-resolved in the fs-TA or ns-TA experiments. However, in fs-TA the decay of spectral features associated with radical cations is much faster (<50 ps), suggesting another scenario where the radical cation is reduced with solvated electrons resulting in the formation of the initial naphthol molecule in its ground state. Still, phenoxyl radicals could be formed on nanosecond time scales *via* a homolytic O—H cleavage reactions [49]. In the system there are no obvious H-atom acceptors, but a solvent such as CH_3CN may act as a H-atom acceptor, and these O—H cleavage reactions are well-documented in the photochemistry of phenols [48]. To verify the assignment of the transient at 360 nm, we performed quenching experiments with ascorbate, which is a known quencher of phenoxyl radicals [50]. Results are shown in Figs. S6 and S7 where it can be seen how adding ascorbic acid not only shortens the lifetime of the 350 nm transient but also decreases its intensity, which means that, besides quenching the 350 nm transient, adding ascorbic acid also quenches its precursor. We have also performed fluorescence quenching experiment in which we demonstrated that ascorbic acid quenches fluorescence of **1** (see Figs. S9 and S10 in the Supporting Information). Note, however, that ascorbic acid absorbs at 266 nm, which is the main reason for a weaker intensity of the transient absorption signal. Since it is plausible to propose that ascorbic acid does not have any impact on a benzoxete, our findings suggest an alternative assignment of the QM precursor at 360 nm to a phenoxyl radical which after an elimination of OH· produces **1-QM**. Note that such a mechanism has been proposed for the formation of QMs from anthrols, [51] and 2,6-substituted naphthols [30].

Transient absorption spectra of **2** [30] are considerably different compared to those of **1** and indicate no other intermediates appearing in the time window from 1.1 ns to a few tens of nanoseconds that was not covered by fs-TA and LFP data. In the TA spectra of **2** recorded in N_2- or

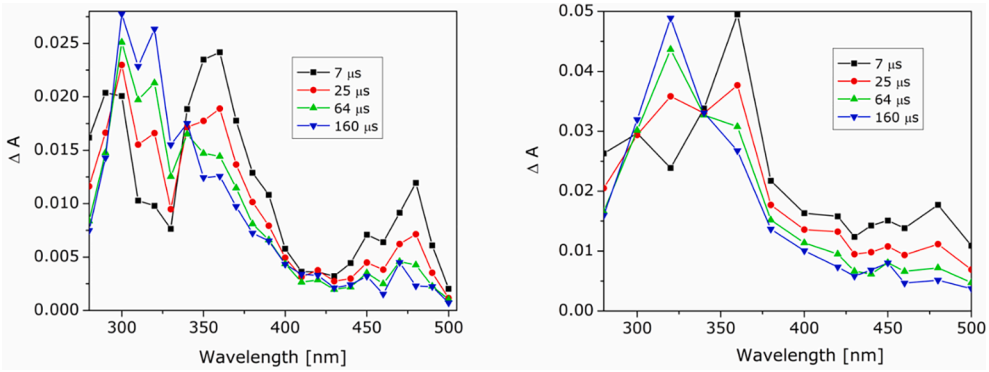

Fig. 10. ns-TA spectra of **1** in O_2-purged CH_3CN (left) and CH_3CN-H_2O (1:1) (right). The transient absorbing around 360 nm decays and gives rise to the transient at 330 nm, which is assigned to QM. Since QM generation takes place on microsecond time scales, it cannot be seen in the fs-TA experiment.

O_2-purged CH_3CN-H_2O (1:1 v/v), a strong absorption band at 370 nm can be seen, with a shoulder at 470 nm (Fig. 11) that decays over ms time scale. The transient coincides with the one detected by fs-TA that was assigned to **2-QM** (S_0). Double structure of the rising band in fs-TA measurements at 350 nm and 370 nm is not visible in LFP measurements in CH_3CN-H_2O due to a decreased spectral resolution. In fs-TA data we assigned a band emerging at 430 nm to a triplet-triplet absorption, which can also be seen in the ns-TA spectra at a short delay time after the laser pulse. This transient is quenched by O_2 (in O_2-purged solution, $k = (1–2) \times 10^7$ s^{-1}, τ = 20–60 ns, see Fig. S8) [30].

Unlike the TA measurements for **2** where the QM generation was observed in fs-TA experiment and its decay in LFP measurements, for **1** the QM generation is observed on microsecond time scales.

3.6. Computational study and the photochemical reaction mechanism

Our experimental findings were complemented with a TD-DFT computational study of QM generation from **1** and **2**. Stationary points for the ground and the first excited state of both molecules were computed at the PCM(water)/(TD-)ωB97XD/6–311++G(d,p) level of theory. Schematic representations of the obtained computational results are shown in Figs. 12 and 13. Since the fs-TA experimental results indicate that **2-QM** is formed directly from **2**(S_1) without an intermediate structure, a CI pathway is the most probable one. Moreover, the failure to adiabatically optimize the transition state **2-TS**(S_1) also indirectly points toward a presence of a CI since TD-DFT methods in general encounter problems when faced with CI geometries. However, an implementation in the Orca 4.2.0 program [39] enables simultaneous optimization of the ground and first excited state of the target structure in a way that facilitates a close approach toward the CI region, essentially confirming a reaction pathway through a CI. In order to scan the potential energy surface of **2** for such a path, we performed a CI optimization of the ground and the first excited state geometries and found the energy difference between them to amount to only 1.0 kcal mol^{-1} for **2** and 3.4 kcal mol^{-1} for **1**. Thus, the energy difference between the geometries found for **2** is small enough to confirm the presence of the CI and therefore points towards **2-QM**(S_0) formation directly from **2**(S_1) without any intermediates (See SI, Table S7).

Fig. S12 shows simulated absorption spectrum of **2-QM**(S_0). Absorption bands peaking at around 315 nm and 530 nm most probably fall within spectral range covered by fs-TA and LFP measurements and could correspond to double structured band with maxima at 350 and 370 nm observed in fs-TA and a 470 nm band that was resolved only in LFP measurements covering longer time scales. Since TD-DFT methods have known limitations in predicting accurate theoretical spectral band positions, this result can be considered qualitatively satisfying since it matched similar spectral shape and intensity ratio to the experimental one with relatively small shifts in absorption maxima.

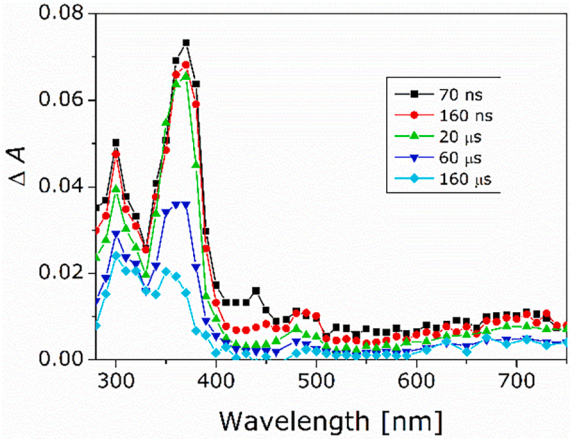

Fig. 11. ns-TA spectra of **2** in O_2-purged CH_3CN-H_2O (1:1 v/v). Absorption bands at 370 nm and 470 nm, assigned to QM, decay on microsecond scales with no other intermediates rising.

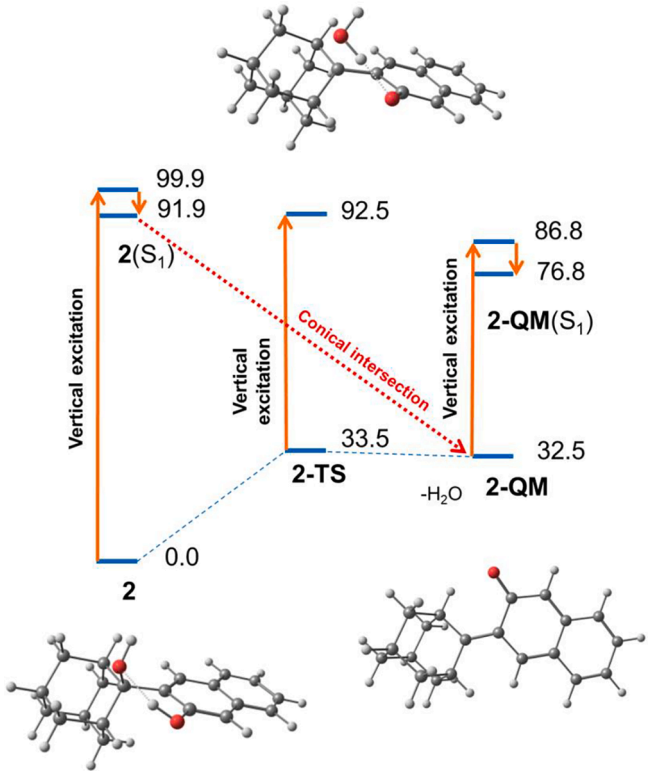

Fig. 12. Mechanism considerations of QM formation from **2**. Stationary points for the ground and the first excited state were computed at the PCM(water)/(TD-)ωB97XD/6–311++G(d,p) level of theory. Relative energies are given in kcal mol^{-1} and energy difference corresponding to conical intersection amounts to 1.0 kcal mol^{-1}. Vertical excitation energy from S_0 to S_1 corresponds to theoretical 286 nm for **2** and to 526 nm for **2-QM**.

Energy diagram obtained for compound **1** is shown in Fig. 13 where it can be observed that the benzoxete **1-BO**(S_1) lies energetically out of reach as the energy difference with respect to naphthol **1**(S_1) amounts to ≈30 kcal mol^{-1}. Computed energy difference between the ground and the first excited state of **1-BO** totals to ≈100 kcal mol^{-1}, which corresponds to approximately 285 nm. This is significantly out of our wavelength detection range, thus making the potential benzoxete species unobservable using our fs-TA experimental set-up. Additionally, this energy diagram also indicates possible QM formation pathway from a radical **1-R** where stationary points were computed at the same level of theory as mentioned before. Phenoxyl radical **1-R** with a relative energy of 88.7 kcal mol^{-1} lies ≈4 kcal mol^{-1} lower in energy with respect to **1** (S_1), which makes it a highly probable intermediate in this reaction. Thus, considering the presented experimental and theoretical findings, we propose a pathway of the reaction going through a phenoxyl radical as an intermediate in the generation of **1-QM** from **1**.

On the basis of all the information we acquired on the photochemistry of investigated naphthols we finally propose two distinct reaction pathways where adamantyl-naphthol **2** undergoes a non-adiabatic excited state intramolecular proton transfer (ESIPT) coupled with dehydration *via* a conical intersection, resulting in the QM formation (Scheme 3). In photodehydration reaction of naphthol **1** (Scheme 4), after initial ultrafast internal conversion of the excited molecule, related radical cation is reduced with solvated electrons, resulting in a back electron transfer and the reformation of the initial naphthol molecule. Here, QMs are generated from phenoxyl radicals formed in a H-transfer reaction after the elimination of OH·.

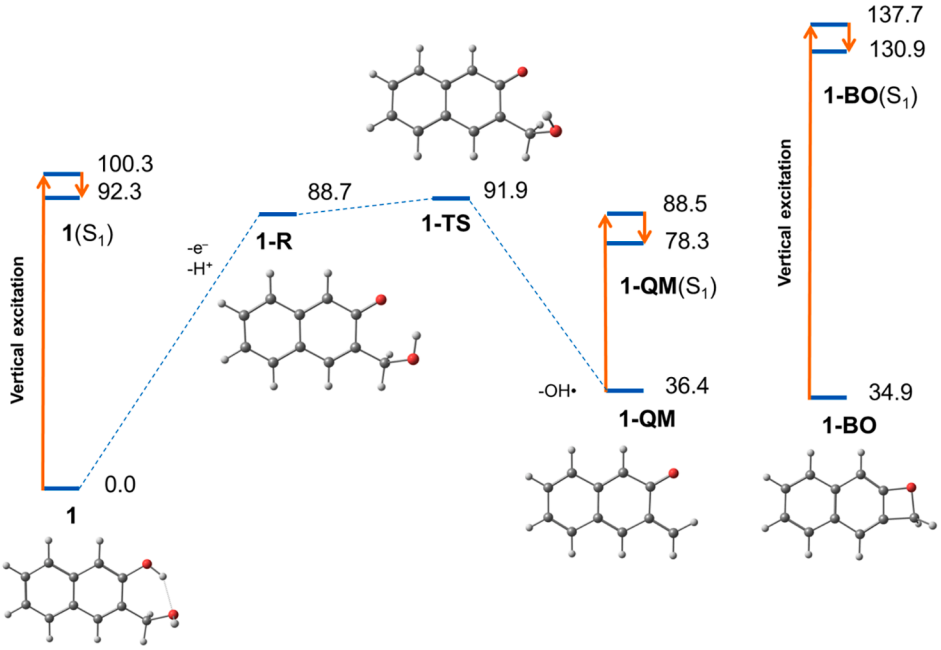

Fig. 13. Mechanism considerations of QM formation from **1**. Stationary points for the ground and the first excited state were computed at the PCM(water)/(TD-)ω B97XD/6–311++G(d,p) level of theory. Relative energies are given in kcal mol^{-1}. Vertical excitation energy from S_0 to S_1 corresponds to theoretical 285 nm for **1** and to 549 nm for **1-QM**.

4. Conclusions

In order to elucidate the mechanism of QM generation, photochemical reaction pathways for two 2-naphthol derivatives sharing an identical chromophore were monitored on different time scales. Following UV excitation, adamantyl-naphthol **2** undergoes a non-adiabatic excited state intramolecular proton transfer (ESIPT) coupled with dehydration *via* a conical intersection, resulting in the observed QM formation within the first few nanoseconds (Scheme 3). On the other hand, for naphthol **1** in fs-TA data on nanosecond time scale, in addition to internal conversion of the excited molecule, only formation and relatively fast decay of radical cation was observed. Since deprotonation of radical cations usually takes place on longer time scales of hundreds of picoseconds up to few nanoseconds [42] < 50 ps decay at relevant wavelengths (380 nm and 570 nm) suggests that radical cation is reduced with solvated electrons, resulting in a back electron transfer and the reformation of the initial naphthol molecule in its ground state. We therefore conclude that photoionization and radical cation formation lead to a competing process that is not directly connected to the photochemical reaction of QM formation. On the other hand, a phenoxyl radical (360 nm band in LFP data) that we identified as a QM precursor could be formed in a H-transfer reaction (Scheme 4) that is known to evolve on nanosecond time scales [48]. In this case, formation of the phenoxyl radical cannot be resolved with fs-TA that covers only nanosecond time-window or in LFP measurements that use 10 ns excitation pulses. The phenoxyl radical undergoes elimination of OH·, delivering also the QM, but in a significantly slower process that takes place over microseconds.

Our combined experimental and computational approach unraveled mechanistic details for the photodehydration reaction in 2-naphthol derivatives. We have demonstrated that introduction of a simple alkyl substituent such as adamantane into the chromophore changes photochemical pathways by lowering the energy gap between the S_1 and S_0 surfaces, enabling a photochemical pathway *via* a conical intersection. Without such a conical intersection, 2-naphthol derivatives undergo photodehydration, but *via* an alternative slower process involving phenoxyl radicals.

CRediT authorship contribution statement

Mateo Forjan: Writing – original draft, Formal analysis, Data curation. **Silvije Vdović:** Writing – original draft, Supervision, Funding acquisition, Conceptualization. **Marina Šekutor:** Software, Methodology, Formal analysis, Conceptualization. **Đani Škalamera:** Validation, Resources. **Piotr Kabaciński:** Formal analysis, Data curation. **Giulio Cerullo:** Writing – original draft, Project administration, Methodology, Conceptualization.

Declaration of Competing Interest

The authors declare that they have no known competing financial interests or personal relationships that could have appeared to influence the work reported in this paper.

Data availability

Data will be made available on request.

Acknowledgements

This work has been supported in part by the Croatian Science Foundation's funding of the project UIP-05-2017-5831. The research was sponsored in part by European Union's Horizon 2020 research and innovation programme under grant agreement no 654148 Laserlab-Europe. M.Š. thanks Professor Peter R. Schreiner for kindly providing computational resources of the Justus-Liebig-University, Giessen, Germany.

Appendix A. Supplementary data

Supplementary data to this article can be found online at https://doi.org/10.1016/j.jphotochem.2022.114171.

References

[1] S.E. Rokita. *Quinone Methides*, Wiley, Hoboken, 2009.

[2] P. Wang, Y. Song, L. Zhang, H. He, X. Zhou, Quinone methide derivatives: important intermediates to DNA alkylating and DNA cross-linking actions, Curr. Med. Chem. 12 (2005) 2893–2913.
[3] M. Frecero, Quinone methides as alkylating and cross-linking agents, Mini Rev. Org. Chem. 1 (2004) 403–415.
[4] M.S. Singh, A. Nagaraju, N. Anand, S. Chowdhury, *ortho*-quinone methide (*o*-QM): a highly reactive, ephemeral and versatile intermediate in organic synthesis, RSC Adv. 4 (2014) 55924–55959.
[5] W.-J. Bai, J.G. David, Z.-G. Feng, M.G. Weaver, K.-L. Wu, T.R.R. Pettus, The domestication of *ortho*-quinone methides, Acc. Chem. Res. 47 (2014) 3655–3664.
[6] P. Pande, J. Shearer, J. Yang, W.A. Greenberg, S.E. Rokita, Alkylation of nucleic acids by a model quinone methide, J. Am. Chem. Soc. 121 (1999) 6773–6779.
[7] W.F. Veldhuyzen, A.J. Shallop, R.A. Jones, S.E. Rokita, Thermodynamic versus kinetic products of DNA alkylation as modeled by reaction of deoxyadenosine, J. Am. Chem. Soc. 123 (2001) 11126–11132.
[8] H. Wang, M.S. Wahi, S.E. Rokita, Immortalizing a transient electrophile for DNA cross-linking, Angew. Chem. Int. Ed. 47 (2008) 1291–1293.
[9] H. Wang, S.E. Rokita, Dynamic cross-linking is retained in duplex DNA after multiple exchange of strands, Angew. Chem. Int. Ed. 49 (2010) 5957–5960.
[10] C.S. Rossiter, E. Modica, D. Kumar, S.E. Rokita, Few constraints limit the design of quinone methide-oligonucleotide self-adducts for directing DNA alkylation, Chem. Commun. 47 (2011) 1476–1478.
[11] M. Di Antonio, F. Doria, S.N. Richter, C. Bertipaglia, M. Mella, C. Sissi, M. Palumbo, M. Freccero, Quinone methides tethered to naphthalene diimides as selective G-quadruplex alkylating agents, J. Am. Chem. Soc. 131 (2009) 13132–13141.
[12] M. Nadai, F. Doria, M. Di Antonio, G. Sattin, L. Germani, C. Percivalle, M. Palumbo, S.N. Richter, M. Freccero, Naphthalene diimide scaffolds with dual reversible and covalent interaction properties towards g-quadruplex, Biochimie 93 (2011) 1328–1340.
[13] F. Doria, M. Nadai, M. Folini, M. Di Antonio, L. Germani, C. Percivalle, C. Sissi, N. Zaffaroni, S. Alcaro, A. Artese, S.N. Richter, M. Freccero, Hybrid ligand-alkylating agents targeting telomeric G-quadruplex structures, Org. Biomol. Chem. 10 (2012) 2798–2806.
[14] F. Doria, M. Nadai, M. Folini, M. Scalabrin, L. Germani, G. Sattin, M. Mella, M. Palumbo, N. Zaffaroni, D. Fabris, M. Freccero, S.N. Richter, Targeting loop adeninesin G-quadruplex by a selective oxirane, Chem. Eur. J. 19 (2013) 78–81.
[15] E. Modica, R. Zanaletti, M. Freccero, M. Mella, Alkylation of amino acids and glutathione in water by o-quinone methide. Reactivity and selectivity, J. Org. Chem. 66 (2001) 41–52.
[16] P.G. McCracken, J.L. Bolton, G.R.J. Thatcher, Covalent modification of proteins and peptides by the quinone methide from 2-*tert*-Butyl-4,6-dimethylphenol: selectivity and reactivity with respect to competitive hydration, J. Org. Chem. 62 (1997) 1820–1825.
[17] S. Arumugam, J. Guo, N.E. Mbua, F. Friscourt, N. Lin, E. Nekongo, G.-J. Boons, V. V. Popik, Selective and reversible photochemical derivatization of cysteine residues in peptides and proteins, Chem. Sci. 5 (2014) 1591–1598.
[18] R. Pérez-Ruiz, O. Molins-Molina, E. Lence, C. González-Bello, M.A. Miranda, M. Consuelo Jiménez, Photogeneration of quinone methides as latent electrophiles for lysine targeting, J. Org. Chem. 83 (2018) 13019–13029.
[19] K. Zlatić, I. Antol, L. Uzlac, A.-M. Mikecin Dražić, M. Kralj, C. Bohne, N. Basarić, Labeling of proteins by BODIPY-quinone methides utilizing anti-kasha photochemistry, ACS Appl. Mater. Interfaces 12 (2020) 347–351.
[20] M.M. Toteva, J.P. Richard, The generation and reactions of quinone methides, Adv. Phys. Org. Chem. 45 (2011) 39–91.
[21] N. Basarić, K. Mlinarić-Majerski, M. Kralj, Quinone methides: photochemical generation and its application in biomedicine, Curr. Org. Chem. 18 (2014) 3–18.
[22] C. Percivalle, F. Doria, M. Freccero, Quinone methides as DNA alkylating agents: an overview on efficient activation protocols for enhanced target selectivity, Curr. Org. Chem. 18 (2014) 19–43.
[23] L. Diao, C. Yang, P. Wan, Quinone methide intermediates from the photolysis of hydroxybenzyl alcohols in aqueous solution, J. Am. Chem. Soc. 117 (1995) 5369–5370.
[24] Đ. Škalamera, I. Antol, K. Mlinarić-Majerski, H. Vančik, D.L. Phillips, J. Ma, N. Basarić, Ultrafast adiabatic photodehydration of 2-hydroxymethylphenol and the formation of quinone methide, Chem. Eur. J. 24 (2018) 9426–9435.
[25] S. Arumugam, V.V. Popik, Photochemical generation and the reactivity of o-naphthoquinone methides in aqueous solutions, J. Am. Chem. Soc. 131 (2009) 11892–11899.
[26] S. Arumugam, V.V. Popik, Light-induced hetero-diels alder cycloaddition: a facile and selective photoclick reaction, J. Am. Chem. Soc. 133 (2011) 5573–5579.
[27] S. Arumugam, V.V. Popik, Patterned surface derivatization using diels-alder photoclick reaction, J. Am. Chem. Soc. 133 (2011) 15730–15736.
[28] S. Arumugam, V.V. Popik, Attach, remove, or replace: reversible surface functionalization using thiol-quinone methide photoclick chemistry, J. Am. Chem. Soc. 134 (2012) 8408–8411.
[29] S. Arumugam, S.V. Orski, J. Locklin, V.V. Popik, Photoreactive polymer brushes for high-density patterned surface derivatization using a diels-alder photoclick reaction, J. Am. Chem. Soc. 134 (2012) 179–182.
[30] J. Veljković, L. Uzelac, K. Molcanov, K. Mlinaric-Majerski, M. Kralj, P. Wan, N. Basaric, Sterically congested adamantylnaphthalene quinone methides, J. Org. Chem. 77 (2012) 4596–4610.
[31] M. Forjan, G. Zgrablić, S. Vdović, M. Šekutor, N. Basarić, P. Kabacinski, N.H. M. Pashaki, H.-M. Frey, A. Cannizzo, G. Cerullo, Photogeneration of quinone methide from adamantylphenol in an ultrafast non-adiabatic dehydration reaction, Phys. Chem. Chem. Phys. 24 (2022) 4384–4393.
[32] C. Slavov, H. Hartmann, J. Wachtveitl, Implementation and evaluation of data analysis strategies for time-resolved optical spectroscopy, Anal. Chem. 87 (2015) 2328–2336.
[33] R. Borrego-Varillas, L. Ganzer, G. Cerullo, C. Manzoni, Ultraviolet transient absorption spectrometer with Sub-20-fs time resolution, Appl. Sci. 8 (2018) 989.
[34] Gaussian 16, Revision B.01, Frisch, M. J.; Trucks, G. W.; Schlegel, H. B.; Scuseria, G. E.; Robb, M. A.; Cheeseman, J. R.; Scalmani, G.; Barone, V. ; Petersson, G. A.; Nakatsuji, H.; Li, X.; Caricato, M.; Marenich, A. V.; Bloino, J.; Janesko, B. G.; Gomperts, R. ; Mennucci, B.; Hratchian, H. P.; Ortiz, J. V.; Izmaylov, A. F.; Sonnenberg, J. L.; Williams-Young, D.; Ding, F.; Lipparini, F.; Egidi, F.; Goings, J.; Peng, B.; Petrone, A.; Henderson, T.; Ranasinghe, D.; Zakrzewski, V. G.; Gao, J.; Rega, N.; Zheng, G.; Liang, W.; Hada, M.; Ehara, M.; Toyota, K.; Fukuda, R.; Hasegawa, J.; Ishida, M.; Nakajima, T.; Honda, Y.; Kitao, O.; Nakai, H.; Vreven, T.; Throssell, K.; Montgomery, J. A. Jr.; Peralta, J. E.; Ogliaro, F.; Bearpark, M. J.; Heyd, J. J.; Brothers, E. N.; Kudin, K. N.; Staroverov, V. N.; Keith, T. A.; Kobayashi, R.; Normand, J.; Raghavachari, K.; Rendell, A. P.; Burant, J. C.; Iyengar, S. S.; Tomasi, J.; Cossi, M.; Millam, J. M.; Klene, M.; Adamo, C.; Cammi, R.; Ochterski, J. W.; Martin, R. L.; Morokuma, K.; Farkas, O.; Foresman, J. B.; Fox, D. J. Gaussian, Inc., Wallingford CT, 2016.
[35] J.-D. Chai, M. Head-Gordon, Long-range corrected hybrid density functionals with damped atom-atom dispersion corrections, Phys. Chem. Chem. Phys. 10 (2008) 6615–6620.
[36] J. Tomasi, B. Mennucci, R. Cammi, Quantum mechanical continuum solvation models, Chem. Rev. 105 (2005) 2999–3093.
[37] J. Ma, M. Šekutor, Đ. Škalamera, N. Basarić, D.L. Phillips, Formation of quinone methides by ultrafast photodeamination: a spectroscopic and computational study, J. Org. Chem. 84 (2019) 8630–8637.
[38] F. Neese, The ORCA program system, WIREs Comput. Mol. Sci. 2 (2012) 73–78.
[39] F. Neese, Software update: the ORCA program system, version 4.0, *WIREs Comput*, Mol. Sci. 8 (2017) e1327.
[40] J. Turro, V. Ramamurthy, J.C. Scaiano, Modern Molecular Photochemistry of Organic Molecules, University Science Books, Sausalito California, 2010.
[41] J.J. Snellenburg, S.P. Laptenok, R. Seger, K.M. Mullen, I.H. van Stokkum, Glotaran: a java-based graphical user interface for the R package TIMP, J. Stat. Sotfw. 49 (2012) 1–22.
[42] H. Mohan, R. Hermann, S. Naumov, J.P. Mittal, O. Brede, Two channels of electron transfer observed for the reaction of n-butyl chloride parent radical cations with naphthols and hydroxybiphenyls, J. Phys. Chem. A 102 (1998) 5754–5762.
[43] T.A. Gadosy, D. Shukla, L.J. Johnston, Generation, characterization, and deprotonation of phenol radical cations, J. Phys. Chem. A 103 (1999) 8834–8839.
[44] I. Carmichael, G.L. Hug, Triplet–triplet absorption spectra of organic molecules in condensed phases, J. Phys. Chem. Ref. Data 15 (1986) 1–250.
[45] N. Basarić, I. Žabčić, K. Mlinarić-Majerski, P. Wan, Photochemical formation and chemistry of long-lived adamantylidene-quinone methides and 2-adamantyl cations, J. Org. Chem. 75 (2010) 102–116.
[46] M.H. Kleinman, J.H. Flory, D.A. Tomalia, N.J. Turro, Effect of protonation and PAMAM dendrimer size on the complexation and dynamic mobility of 2-naphthol, J. Phys. Chem. B 104 (2000) 11472–11479.
[47] L. Pretali, F. Doria, D. Verga, A. Profumo, M. Freccero, Photoarylation/alkylation of bromonaphthols, J. Org. Chem. 74 (2009) 1034–1041.
[48] G. Siano, S. Crespi, S.M. Bonesi, Direct irradiation of phenol and para-substituted phenols with a laser pulse (266 nm) in homogeneous and micro-heterogeneous media. A time-resolved spectroscopy study, J. Org. Chem. 85 (2020) 14012–14025.
[49] E.J. Land, G. Porter, Primary photochemical processes in aromatic molecules. Part 7. —Spectra and kinetics of some phenoxyl derivatives, Trans. Farad. Soc. 59 (1963) 2016–2026.
[50] P. Neta, J. Grodkowski, Rate constants for reactions of phenoxyl radicals in solution, J. Phys. Chem. Ref. Data 34 (2005) 109–199.
[51] Đ. Škalamera, K. Mlinarić-Majerski, I. Martin Kleiner, M. Kralj, J. Oake, P. Wan, C. Bohne, N. Basarić, Photochemical Formation of Anthracene Quinone Methide Derivatives, J. Org. Chem. 82 (2017) 6006–6021.